Scanning AC Nanocalorimetry Study of Zr/B Reactive Multilayers

Scanning AC nanocalorimetry study of Zr/B reactive multilayers

Dongwoo Lee[1], Gi-Dong Sim[1] , Kechao Xiao[1] , Yong Seok Choi [1,2], and Joost J. Vlassak[1,a]

[1] School of Engineering and Applied Sciences, Harvard University, Cambridge, Massachusetts 02138, USA

[2] Department of Materials Science and Engineering, Seoul National University, Seoul 151-742, South Korea.

Abstract

The reaction of Zr/B multilayers with a 50 nm modulation period has been studied using scanning AC nanocalorimetry at a heating rate of approximately 10^3 K/s. We describe a data reduction algorithm to determine the rate of heat released from the multilayer. Two different exothermic peaks are identified in the nanocalorimetry signal: a shallow peak at low temperature (200 - 650°C) and a sharp peak at elevated temperature (650 - 800°C). TEM observation shows that the first peak corresponds to heterogeneous inter-diffusion and amorphization of Zr and B, while the second peak is due to the crystallization of the amorphous Zr/B alloy to form ZrB_2.

Keywords: ZrB2, multilayer, scanning AC nanocalorimetry, ultra high temperature ceramic

[a)] e-mail address: vlassak@seas.harvard.edu

I. Introduction

ZrB_2, classified as an ultra high-temperature ceramic (UHTC), possesses superb thermal, mechanical, and electrical properties, including an extremely high melting point (>3200 °C), high thermal/electric conductivity, chemical inertness, excellent thermal shock resistance, and good oxidation resistance. Due to these benefits, the utilization of this transition metal boride has been proposed for advanced structural applications in extreme environments, such as wing leading edges, nose tips, and propulsion system components of hypersonic vehicles [1-3].

The unique set of properties of ZrB_2 stem mainly from the highly covalent nature of the Zr-B and B-B bonding, and the ionic nature of Zr-Zr bonding in the hexagonal closed packed structure (P6/mmm) [1, 4]. ZrB_2 can be prepared using reactive processes, including self-propagating high-temperature synthesis (SHS), spark plasma synthesis (SPS), and reactive hot pressing (RHP). Chemical routes and reduction processes are also available for the preparation of ZrB_2 [1]. Regardless of the type of processing methods, fabrication of dense structure of ZrB_2 requires very high temperature and pressure, which makes processing difficult [1, 5].To overcome challenges such as poor sinterability and difficult densification, and to investigate the thermo-physical characteristics of the material, a great deal of research has been devoted to phase/structure evolution and chemical composition change during ZrB_2 formation. [6-10]. In this study we employ scanning AC nanocalorimetry to investigate the synthesis of ZrB_2 from reactive multilayers of Zr and B.

Calorimetry of multilayered thin-film materials systems can be used to conduct fundamental studies of the thermodynamics and kinetics of reactions that are not readily accessible in bulk materials systems. [11-15]. Nanocalorimetry makes it possible to conduct such studies on extremely small samples over a very wide range of heating rates [15-20]. DC nanocalorimetry, in particular, can be used to make accurate calorimetry measurements at heating and cooling rates in the 4,000-40,000 K/s range, whereas AC

nanocalorimeters were developed [20-23] to enable measurements for scan rates below 4,000K/s, bridging the gap between traditional calorimetry and DC nanocalorimetry.

When multilayers with large negative reaction enthalpies react, they release a large amount of thermal energy that can be used for joining two dissimilar materials. For example, nano-structured Ni/Al multilayers have been studied to braze various materials including alloys, bulk metallic glass, and silicon [24-28]. In this process, the Ni/Al multilayer acts as a local heat source that melts the brazing layers. A small thermal pulse is sufficient to activate the brazing process because the large enthalpy of reaction of Ni and Al, and the short diffusion distances in the multilayer lead to a self-propagating reaction. As the reaction to form ZrB_2 from Zr and B is highly exothermic [4], it may be possible to use nano-structured multilayers of Zr and B for joining materials, especially in ultra high-temperature applications. This potential application motivated us to investigate the solid-state reaction in Zr/B multilayers.

The aim of this paper is two-fold: 1) the first application of scanning AC nanocalorimetry to a reactive multilayer sample at a heating rate that is not accessible with traditional calorimetry, and 2) investigation of the solid-state reaction in Zr/B multilayers upon heating. We discuss the experimental details of scanning AC nanocalorimetry in Sec. II, III, and V. In Sec. IV, we propose a data reduction method to extract the rate of heat release from the multilayer sample and we verify its validity using finite element simulations. In Sec. VI, we present the results of the scanning AC nanocalorimetry study of a Zr/B multilayer and show that the formation of ZrB_2 proceeds in a two-step process.

II. The nanocalorimetry sensor

Scanning nanocalorimetry measurements were performed on a thin Zr/B multilayer using the parallel nano-scanning calorimeter device (PnSC) [18, 19]. This device consists of an array of nanocalorimeter sensors capable of thermo-physical characterization of samples with very small thermal mass. As schematically drawn in Fig. 1, each sensor in a PnSC device consists of a metal line encapsulated in a thin non-conducting membrane. The metal line serves both as a heater and as a resistive thermometer in a four-point measurement scheme. During a calorimetry measurement, a current is applied to the metal line and the line heats the sample of interest. Both the applied current and the voltage drop

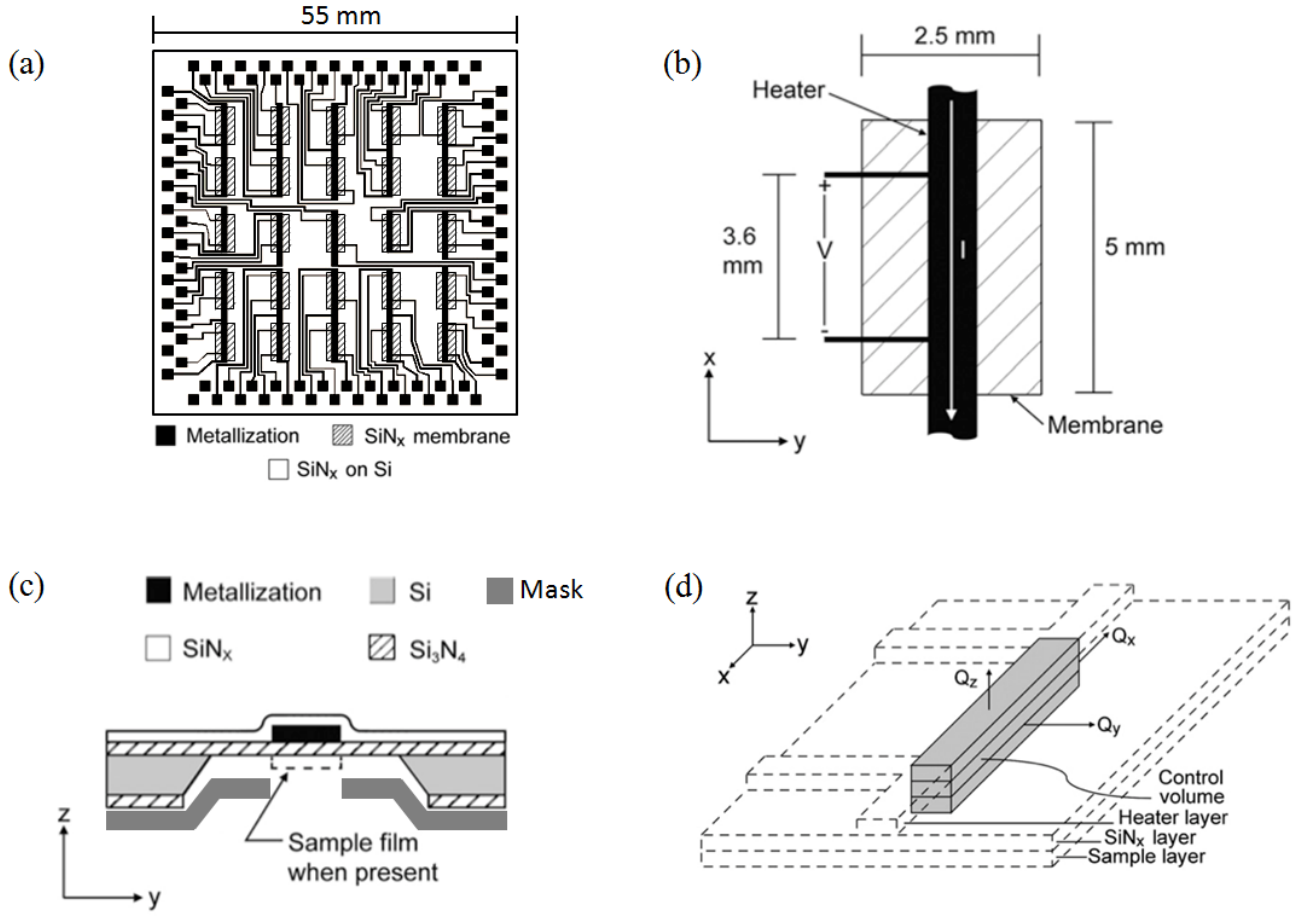

Fig. 1. Schematic of the PnSC device. (a) Plan view of the PnSC device showing an array of nanocalorimetry sensors; (b) plan view of one sensor; (c) cross-sectional view of a sensor; (d) perspective view of the control volume containing sample and sensor addendum.

across the resistance thermometer are continuously recorded, enabling precise measurement of the power supplied to the sensor and the temperature of the sample, which is related to the resistance of the heating element by

$$R(T_0) = R(T_A)(1 + \lambda(T_0 - T_A)) \quad (1)$$

where R is the resistance of the heating element, λ is the temperature coefficient of resistance of the line, T_0 is the average temperature of the heating element, and T_A denotes the ambient temperature. In a typical measurement, the thermal diffusion lengths of sample and membrane are much larger than their thicknesses, making any temperature gradients in the out-of-plane direction negligibly small [18, 19].

III. Scanning AC nanocalorimetry

The nanocalorimetric sensors on the PnSC device can be used to perform either DC or AC measurements depending on the heating rate. DC nanocalorimtery requires a high heating rate (1,000 - 40,000 K/s) to minimize any heat loss to the environment. AC nanocalorimetry, on the other hand, is insensitive to heat loss and can be used at heating rates ranging from isothermal to 4,000K/s [20-23].

When a current I is supplied to the heating element of a PnSC sensor, the energy balance for the control volume (CV) that contains the sample and sensor addendum as marked in Fig. 1d is

$$P = I^2 R$$

$$= C_p \frac{dT}{dt} + L + H \tag{2}$$

where P is the power supplied to the heater, R the resistance of the heating element within the CV, C_p the total heat capacity of the CV, and L the rate of heat loss to the environment. The enthalpy term H represents the rate at which the sample absorbs or releases heat as a result of solid-state reactions or phase transformations. In the context of this paper, we refer to this term as the reaction enthalpy flow. In a DC nanocalorimetry measurement, the heating rate needs to be sufficiently large that the heat loss L is small compared with the other two terms in the right hand side of Eq. (2). Knowledge of the power supplied to the sensor and the heating rate then provides the necessary data to determine the calorimetric signal of the sample. At slow scan rates or very high temperatures, the heat loss to the environment becomes so large that DC measurements fail to give meaningful results. In that case, measurements can be performed by means of scanning AC nanocalorimetry. The scanning AC nanocalorimetry technique is discussed at length in references [20] and [22]; here we provide a brief summary. In scanning AC nanocalorimetry, the sensor is heated with a current that consists of a DC component and an oscillating component with angular frequency ω,

$$I = I_0 + i\cos\omega t. \tag{3}$$

If the frequency is high enough, near-adiabatic operation of the sensor can be achieved enabling one to obtain precise values of the heat capacity. For AC nanocalorimetry, the energy balance equation can be written as

$$P = \left[I_0 + i\cos\omega t\right]^2 R_0(1 + \lambda\theta)$$

$$= C_P\left(\frac{dT_0}{dt} + \frac{d\theta}{dt}\right) + L + H \tag{4}$$

where T_0 is the temperature of the CV averaged over one oscillating period, θ is the oscillating part of the temperature, and R_0 is the resistance of the heating element at temperature T_0. The temperature oscillation of the heater produces harmonics in the potential drop across the resistor that can be used to determine the heat capacity of the sample and sensor [20]. With some mathematical manipulations, Eq. (4) can be written as a set of two equivalent equations in T_0 and θ.

$$P_0 = \left({I_0}^2 + \frac{1}{2}i^2\right)R_0 = C_P\frac{dT_0}{dt} + L_0 + H_0, \tag{5}$$

$$2I_0 iR_0\cos\omega t + \frac{1}{2}i^2 R_0\cos 2\omega t = C\frac{d\theta}{dt} + \alpha\theta \tag{6}$$

where L_0 and H_0 represent the heat loss and reaction enthalpy flow averaged over one oscillation period, and α is the sum of their total time derivatives. Eq. (5) describes the monotonic temperature response of the sensor, while Eq. (6) describes its oscillatory response. Further analysis of Eq. (6) eventually leads to the following expression for the heat capacity of the CV [20, 22-23] in terms of the measured amplitude $V_{2\omega}$ and phase angle φ of the 2ω - harmonic in the voltage across the resistor:

$$C_P = \frac{i^2 I_0 R_0\lambda}{\omega|V_{2\omega}|}\sqrt{\frac{25\tan^2\varphi+9}{16\tan^2\varphi+4}\times\frac{\tan^2\varphi}{1+\tan^2\varphi}} \tag{7}$$

The phase angle φ and α are related by

$$\tan\varphi = \frac{C_P\omega}{\alpha} \tag{8}$$

These expressions are accurate provided that R_0 remain constant on the time scale of the temperature oscillations and θ be sufficiently small [20],

$$\lambda \frac{dT_0}{dt}\frac{2\pi}{\omega} \ll 1,$$

$$\lambda\theta \ll 1, \tag{10}$$

respectively. These conditions are readily satisfied by designing the input current profile following the procedure detailed in reference [20].

IV. Analysis of solid-state reactions using scanning AC nanocalorimetry

While scanning AC nanocalorimetry allows direct determination of the heat capacity of a sample using Eq. (7), it is also possible to extract information on the enthalpy flow *H* resulting from any solid-state reaction in the sample by considering the DC component of the calorimetry signal. In this section, we describe a simple but effective method to perform this analysis and use a finite element simulation to verify its accuracy.

Consider the following more explicit form of the energy balance in Eq. (5)

$$P_0 = C_p \frac{dT_0}{dt} + L_C(T_0, \chi) + L_R(T_0) + H_0(T_0, \chi), \tag{11}$$

Here, L_C represents the power lost to the environment by conduction through the membrane and the heating element, while L_R represents the radiative heat loss, both quantities appropriately averaged over one oscillation period. Since measurements are typically performed in vacuum, there is no convective heat loss. The period-averaged past temperature history of the CV is represented by χ. The analysis method is based on the observations that the radiative heat loss is a function of temperature only, while the conductive heat loss depends on both temperature and temperature history. Furthermore, for small temperature oscillations, the averaged heat loss terms do not depend on the amplitude of the temperature oscillations. The reaction enthalpy flow, H_0, generally depends on both temperature and past temperature history.

Consider a typical experiment that consists of two subsequent nanocalorimetry scans with similar but not identical heating rates. The sample undergoes an irreversible solid-state reaction during the first scan, but not during the second. The energy balance equations for both scans are then

$$P_0^{(1)}\left(T_0^{(1)}\right) = C_p^{(1)} \frac{dT_0^{(1)}}{dt} + L_C\left(T_0^{(1)}, \chi^{(1)}\right) + L_R\left(T_0^{(1)}\right) + H_0\left(T_0^{(1)}, \chi^{(1)}\right), \tag{12}$$

$$P_0^{(2)}(T_0^{(2)}) = C_p^{(2)}\frac{dT_0^{(2)}}{dt} + L_C\left(T_0^{(2)}, \chi^{(2)}\right) + L_R\left(T_0^{(2)}\right), \tag{13}$$

where the superscripts in parentheses refer to the scan numbers. Taking the difference between both equations for $T_0 = T_0^{(1)} = T_0^{(2)}$, and rearranging the terms leads to the following expression for the reaction enthalpy flow.

$$\begin{aligned} H_0\left(T_0, \chi^{(1)}\right) &= \left(P_0^{(1)}(T_0) - P_0^{(2)}(T_0)\right) - \left(C_p^{(1)}\left(\frac{dT_0}{dt}\right)^{(1)} - C_p^{(2)}\left(\frac{dT_0}{dt}\right)^{(2)}\right) \\ &\quad - \left(L_C\left(T_0, \chi^{(1)}\right) - L_C\left(T_0, \chi^{(2)}\right)\right) \\ &= \Delta P - \Delta\left(C_p\frac{dT_0}{dt}\right) - \Delta L_C, \end{aligned} \tag{14}$$

in which the radiative heat loss term has been eliminated. Each of the terms in the RHS of Eq. (14) is readily evaluated in a typical experiment. The first term represents the difference in power supplied in the two scans and is calculated from the applied current and resistance of the heating element using Eq. (5). The second term arises because the enthalpy of the samples accrues at different rates in the two scans. Since scanning AC nanocalorimetry measurements provide the heat capacity of the CV as a function of temperature, Eq. (7), this term is also easily calculated. Evaluation of this term represents a clear advantage of scanning AC nanocalorimetry over straight DC nanocalorimetry where this term is much more difficult to determine unless the two scans are performed at exactly the same heating rate in a power-compensated scheme and the heat capacity of the CV does not change after the reaction. The last term represents the difference in conductive heat loss as a result of the different temperature histories of the CV during the two scans. This term is well approximated by the following expression

$$L_C\left(T_0(t),\chi^{(1)}\right)-L_C\left(T_0(t),\chi^{(2)}\right)$$

$$=-(2k_mA_m)\frac{\partial}{\partial y}\left(\int_0^t\left(T_0^{(1)}(t')-T_0^{(2)}(t')\right)K_m(t-t')dt'\right)|_{y=0}$$

$$-(2k_hA_h)\frac{\partial}{\partial x}\left(\int_0^t\left(T_0^{(1)}(t')-T_0^{(2)}(t')\right)K_h(t-t')dt'\right)|_{x=0}, \qquad (15)$$

where the subscript *m* refers to membrane properties, while *h* refers to properties obtained by appropriately averaging the heater and membrane properties. A detailed derivation of this expression and the definition of the relevant parameters are found in the Appendix. This expression is evidently somewhat more cumbersome to evaluate. The Appendix also provides a numerical algorithm to accurately evaluate Eq. (15).

In a typical experiment the current supplied to the sensor during the two scans is ramped up at the same rate and the difference in scan rates is caused by the enthalpy associated with a reaction. Consequently, the first term in Eq. (14) arises because the resistance of the heating element is a function of temperature. This term is usually the dominant term in the expression for the reaction enthalpy flow. The difference in conduction heat loss arises solely as a result of the slightly different thermal histories of the scans and is typically quite small; the same is true for the term associated with the enthalpy. The radiative heat loss, which at elevated temperature is often the largest term in Eq. (11), is automatically eliminated, although some care needs to be exercised if the solid-state reaction changes the emissivity of the CV. This effect shows up as a T^4-dependence of the reaction enthalpy flow at high temperatures and, if necessary, can be eliminated by fitting the experimental data over a temperature range where the enthalpy flow is expected to be zero.

To validate the analysis method and the algorithm to calculate the conduction loss, we constructed a finite element model (FEM) of the nanocalorimetry sensor using the commercial software package

COMSOL Multiphysics 4.3a. Typical experiments were simulated using the FEM model and then analyzed using the procedure described above.

TABLE I. Parameters used in the FEM [19, 20].

	Length (mm)	Width (mm)	Thickness (nm)	Heat Capacity $(J/kg \cdot K)$	Thermal Conductivity $(W/m \cdot K)$	Density (kg/m^3)	Emissivity
Membrane	5	2.5	200	700	3.2	3,000	0.18
CV	3.6	0.8	200	291	35.3	15,075	0.04
Heating element	5	0.8	200	267	23.4	12,650	0.04

The FEM model had the same in-plane dimensions as the nanocalorimetry sensor used for the measurements (Fig. 1, Table 1). To save computational time, we constructed a two-dimensional model using properties averaged over the thickness of the sensor, which is a very good approximation for the real sensor since out-of-plane temperature gradients are entirely negligible in a typical measurement. The model was heated by sending a current through heating element. Since most measurements are performed in vacuum, only conductive and radiative heat losses were considered. The thermo-physical parameters of the sensor membrane and heating element used in the model (Table I) were representative for the materials used in the sensors [19, 20]. The electrical resistance of the heating element was modeled as a linearly increasing function of temperature with a value of 8.2 Ω at 24°C and a temperature coefficient of resistance of $0.00115\ K^{-1}$, both values obtained from actual experiments. The emissivity of the top and bottom surfaces of the CV was chosen such that the heating rate in the FEM model was similar to the heating rate obtained in actual measurement. The specific

heat of the CV was selected to make the value equal to that obtained in the measurements. During the simulations, the temperature of the edge of the membrane was fixed at 24°C. Two scans were simulated: one scan in which the sample released enthalpy as a result of a solid-state reaction (scan 1), and one in which it did not (scan 2). The reaction enthalpy released during scan 1 was included in the FEM model as a heat source at the top surface of the CV. The solid-state reaction was modeled as an exothermic two-stage process with a shallow enthalpy peak at low temperature and a sharp peak at elevated temperature. Both peaks were modeled as Gaussian functions of time. The current supplied to the sensor was a DC current equivalent to the current used in the experiments and was given by $I = \sqrt{(15 + 33t)^2 + \frac{1}{2}(12 + 33t)^2}$ mA.

The results of the FEM simulations and the analysis are illustrated in Fig. 2. Fig. 2(a) shows the evolution of the temperature averaged over the CV during both scans. Initially the scans trace each other perfectly, but as the solid-state reaction proceeds the temperature during scan 1 is slightly larger than during scan 2. Fig. 2(b) shows the three terms in the right hand side of Eq. (14) that comprise the reaction enthalpy flow. The terms involving the power and the enthalpy difference can be calculated exactly from experimental data while the conduction loss difference is estimated from Eq. (15). It is evident from the figure that the term associated with the power difference is dominant, while the conduction loss difference is the smallest. Fig. 2(c) displays the conduction loss term as estimated from Eq. (15) using the algorithm described in the Appendix, along with the actual conduction loss difference obtained from the finite element simulations. Eq. (15) provides a good estimate of the conduction loss difference at low temperature but the accuracy is diminished at temperatures in excess of 700°C where radiative loss from the membrane and heating element becomes significant. Given that the difference in conduction loss between the two samples is typically quite small, Eq. (15) provides a reasonable estimate for the conduction correction over the temperature range considered. Fig. 2(d)

shows both the reaction enthalpy determined from an analysis of the FEM results and the reaction enthalpy originally entered into the FEM model. Both curves are evidently in very good agreement, confirming the validity of the analysis. The enthalpies obtained from the FEM analysis and from the proposed method, agree to within 4%. Not taking into account the conduction loss difference increases the error to approximately 7%.

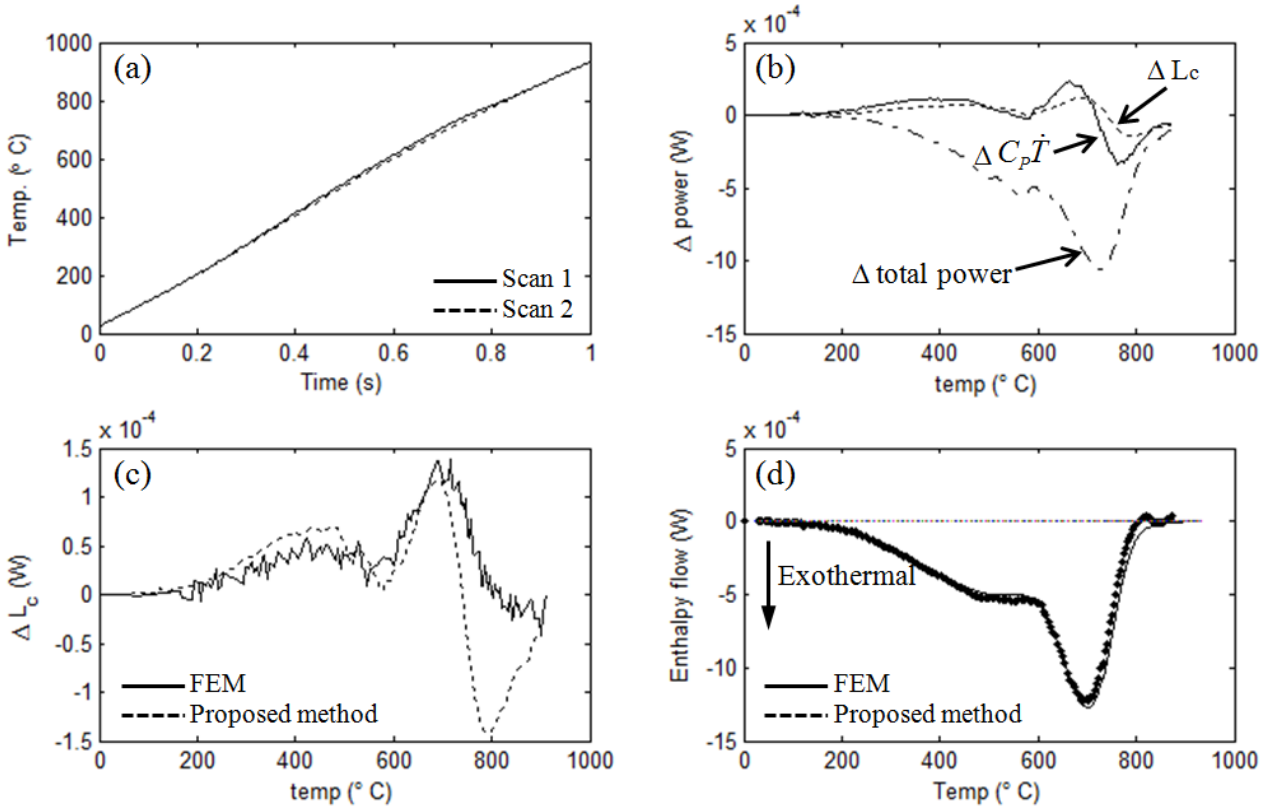

Fig. 2. Validation of the data reduction method using a finite element model: (a) temperature versus time, (b) three power terms in the RHS of Eq. (14), (c) difference in conduction loss versus temperature, and (d) enthalpy flow along with input enthalpy flow.

V. Experimental detail

A. Fabrication and nanocalorimetry measurement

The PnSC device used for the reactive multilayer measurements was fabricated from a (100) single-crystal Si substrate employing standard Si-based micro-fabrication processes as described in detail in references [18, 19]. Each sensor on the PnSC device had a SiN_x membrane and a W heating element. The thickness of the membrane was 200 nm, while that of the heating element was 100 nm.

Before depositing the Zr/B multilayer, the PnSC sensors was stabilized and calibrated. To that effect, the sensors on the PnSC were resistively heated to a temperature of approximately 1000°C, the maximum temperature range used in this study, for a period of 300 ms, and then cooled to room temperature. This thermal cycle resulted in a small shift in the resistance of the heating element because of microstructural changes in the W. This process was repeated until the resistance of the heater stabilized, typically after five thermal cycles. After conditioning, the temperature coefficient of resistance of each cell in the PnSC device was calibrated by heating the PnSC device over a temperature range from 20°C to 120°C in steps of 20°C. These measurements were performed inside a vacuum furnace with Ar gas at ambient pressure to ensure temperature uniformity within the furnace. The temperature coefficient of the resistance was then calculated using Eq. (1).

After calibration of the sensors, Zr/B multilayer samples with a bilayer period of 50 nm were sputter deposited onto three sensors of the PnSC device, one for calorimetry measurements and two for additional transmission electron microscopy (TEM). The total thickness of the multilayers was 100 nm and the thickness of the individual layers was chosen to ensure that the sample would form stoichiometric ZrB_2 upon completion of the reaction. The multilayers were deposited in a sputter chamber with confocal magnetrons (ATC 1800 system, AJA International) and a rotating substrate holder (10 rpm). The base pressure of the chamber was better than 10^{-7} Torr. Zr was deposited at a rate

of 4.7 nm/min using a 99.99% Zr target (Ø 50.8 mm) and a DC power of 80 W. B was deposited at a rate of 0.5 nm/min using a 99.95% B target (Ø 50.8 mm) and an RF power of 150 W. The distance between substrate and targets was 120 mm. The temperature of the substrate was not controlled during the deposition process. To prevent oxidation of the samples during the measurements, the multilayer samples were coated with a 30 nm layer of SiN_x, by reactive sputtering from a Si target (DC 120 W, 5m Torr of Ar) in an N_2 (10sccm) environment.

The samples were deposited through a shadow mask to prevent deposition of material outside of the CV area (Fig. 1a). The shadow mask was fabricated from a vacuum-compatible UV-cross-linkable polymer (VeroWhite, Stratasys Ltd., MN) using an Objet Connex500 3D printer (Stratasys Ltd., MN) in the high-quality print mode. As a result of shadowing by the mask, the thickness of the samples varied 70 nm at the edge to 100 nm in the center, as determined by transmission electron microscopy observation. The mass of the samples was estimated at 1.05 μg from the room-temperature heat capacity, in good agreement with the value determined from the deposition flux and the area of the shadow mask windows.

TABLE II. Summary of the parameters of Zr/B multilayer samples and measurements

DC current, I_0 (mA)	AC current, i (mA)	frequency (Hz)	duration (ms)	heating rate (K/s)
15 – 48	12 - 45	987	1,000	600 - 1,400

Parameters for the scanning AC nanocalorimetry measurements were chosen based on Eqs. (5, 6) and are shown in table II. The calorimetry measurements in this study consisted of two successive scans: scan 1 and scan 2. The multilayer samples reacted during scan 1 and this scan contains the calorimetric signature of the reaction. No reaction took place during scan 2 and this scan was used as a baseline for

the first scan. All nanocalorimetry measurements in this study were performed in vacuum to minimize heat loss to the environment using a custom low-noise data acquisition system described in detail in reference [20]. Typical noise levels in the measurements were on the order of 0.1%. The experimental nanocalorimetry data were analyzed following the data reduction algorithm described earlier; the material parameters used in the analysis were obtained from calibration runs on similar devices [19] and are listed in Table I. The heat capacity of the CV was calculated from the 2ω - harmonic in the voltage across the heating element using Eq. (5).

B. TEM Observation

Cross-sections of the three multilayer samples were investigated by TEM using a JEOL 2010 system operating at 200 KeV. To prepare the TEM samples, 10 µm x 2µm blocks were isolated from the samples of interest using a (30 keV, 150pA) focused beam of Ga ions inside a Zeiss NVision 40 Dual-Beam system. These blocks were attached to an Omniprobe and further thinned to a thickness of approximately 100nm using a 30 KeV, 40pA Ga ion beam inside the FIB. Finally, Ar ion milling was performed in a Nanomill 1040 operating at 500 eV to achieve electron transparency and to remove any Ga ions introduced by the focused ion beam. Each specimen was exposed to the electron beam on both sides for a period of 10 minutes with the gun current set at 140 pA.

VI. Results

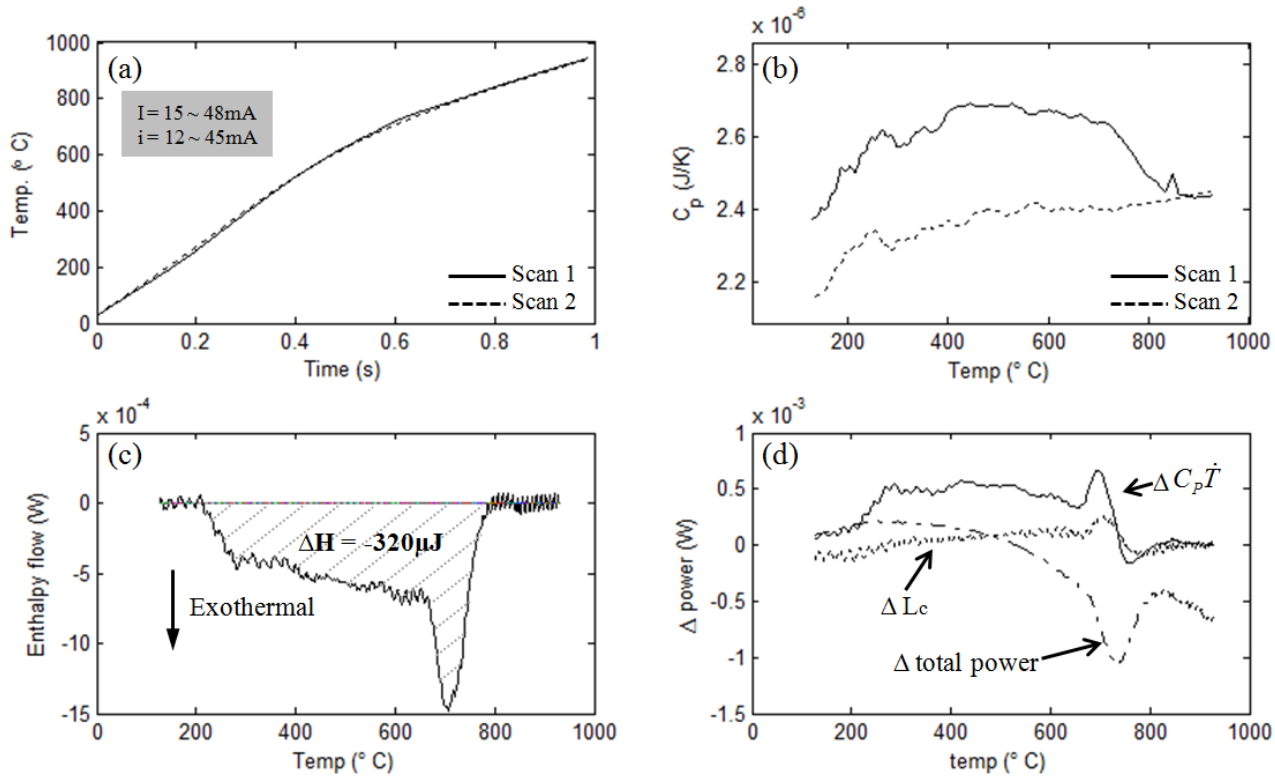

Fig. 3. AC nanocalorimetry measurement results for the Zr/B multilayer: (a) average temperature history, (b) C_p versus temperature obtained from AC measurement, (c) enthalpy flow, and (d) the three terms in the RHS of Eq. (14). To calculate the enthalpy flow a small correction corresponding to a change in emissivity of 2.2% was applied.

A. Nanocalorimetry

The results of the scanning AC nanocalorimetry measurements on the first multilayer sample are depicted in Fig. 3. Fig. 3(a) shows the temperature response of the sample for the two successive scans. Both curves very nearly trace each other with just a few subtle differences: Initially the slope for scan 2 is slightly greater than for scan 1 indicating that the solid-state reaction has reduced the heat capacity of the multilayer sample. Later on, the temperature in scan 1 is slightly larger than in scan 2 because of

the exothermic reaction between Zr and B. At elevated temperatures, the slopes of both temperature curves decline because of significant radiative heat loss. Fig. 3(b) shows the heat capacity of the CV obtained from the 2ω-signal as a function of temperature for both scans. The heat capacity for scan 1 is larger than for scan 2 and increases slightly with temperature until approximately 720°C, when it suddenly decreases to overlap with the heat capacity for scan 2. As will be demonstrated later, this change coincides with the formation of crystalline ZrB_2 in the sample. Fig. 3(c) depicts as a function of temperature the reaction enthalpy flow for the Zr/B multilayer, obtained from the three terms in Fig. 3(d). It is evident from the figure that the reaction in the multilayer proceeds in two stages: there is a broad exothermal peak at low temperature (200 – 650°C), followed by a sharp exothermic peak at more elevated temperature (650 – 800◦C). The total enthalpy of the Zr/B reaction is calculated at -320 μJ by integrating the reaction enthalpy flow with respect to time. Fig. 3(d) shows $\Delta P, \Delta\left(C_p dT_0/dt\right),$ and ΔL_C as a function of temperature. As for the FEM simulations, the power term dominates, while the conduction loss term is quite small. While nanocalorimetry clearly demonstrates that the solid-state reaction in the Zr/B multilayer proceeds in two stages, it does not provide insight in the precise nature of these stages. That insight is provided by TEM analysis of the samples.

B. Transmission Electron Microscopy (TEM)

Fig. 4 shows bright-field TEM micrographs of an unreacted Zr/B multilayer in cross section. The micrographs clearly reveal a crystalline Zr layer (Powder Diffraction File #050665), an amorphous B layer, and an amorphous intermixed layer of Zr and B between them. The thickness of the intermixed layer is approximately 5nm and quite uniform throughout the TEM sample. The Zr layer shows a large

variation in grain size, from a few nanometers (Fig. 4(b)) to a few tens of nanometers (Fig. 4(a)); no grains were detected in the B layers.

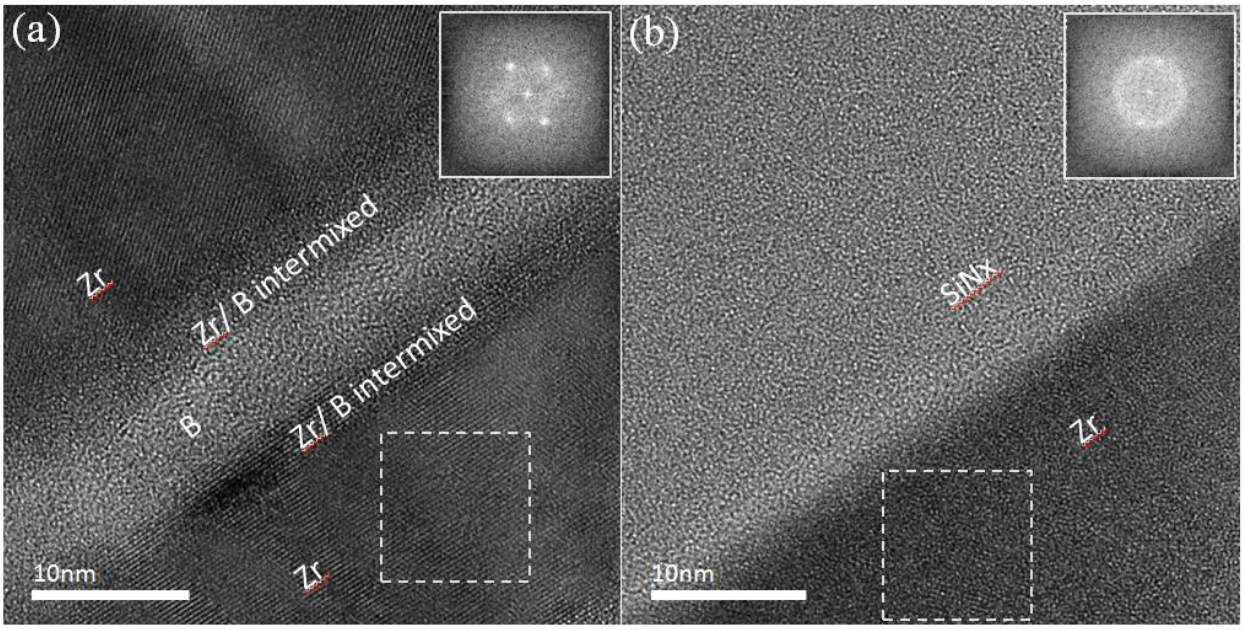

Fig. 4. Cross-sectional transmission electron micrographs of an unreacted Zr/B multilayer. (a) Crystalline Zr layers and an amorphous B layer. Amorphous Zr/B intermixed layers were found between the Zr and B layers. (b) TEM image of a nano-crystalline Zr layer. The inset in each figure is the Fourier transformation of the dashed box in the same figure.

To determine the nature of the two stages in the reaction, a nanocalorimetry measurement was performed on a second Zr/B multilayer sample, interrupting the measurement at a temperature of 450°C, before the second stage of the reaction set in, in essence freezing in the structure that develops during the first stage of the reaction. The corresponding TEM micrographs are shown in Fig. 5. The images show clear inter-diffusion of the Zr and B layers, but in a very heterogeneous fashion: some regions of the TEM specimen have little inter-diffusion (Figs. (a), (d)) and are comparable to the unreacted sample, while other regions show significant inter-diffusion (tens of nanometers as in Figs.

(b), (e), (f)), resulting in the formation of an amorphous Zr-B alloy. This heterogeneous inter-diffusion of Zr and B is not observed in the unreacted sample and indicates that the first stage of the multilayer reaction corresponds to a process of Zr and B inter-diffusion at specific sites along the Zr/B interfaces**.** Only Zr grains were observed in this sample as illustrated by the electron diffraction images in Fig. 5(c); no crystalline ZrB_2 phase was identified. As in the unreacted sample, large variations in Zr grain size were observed.

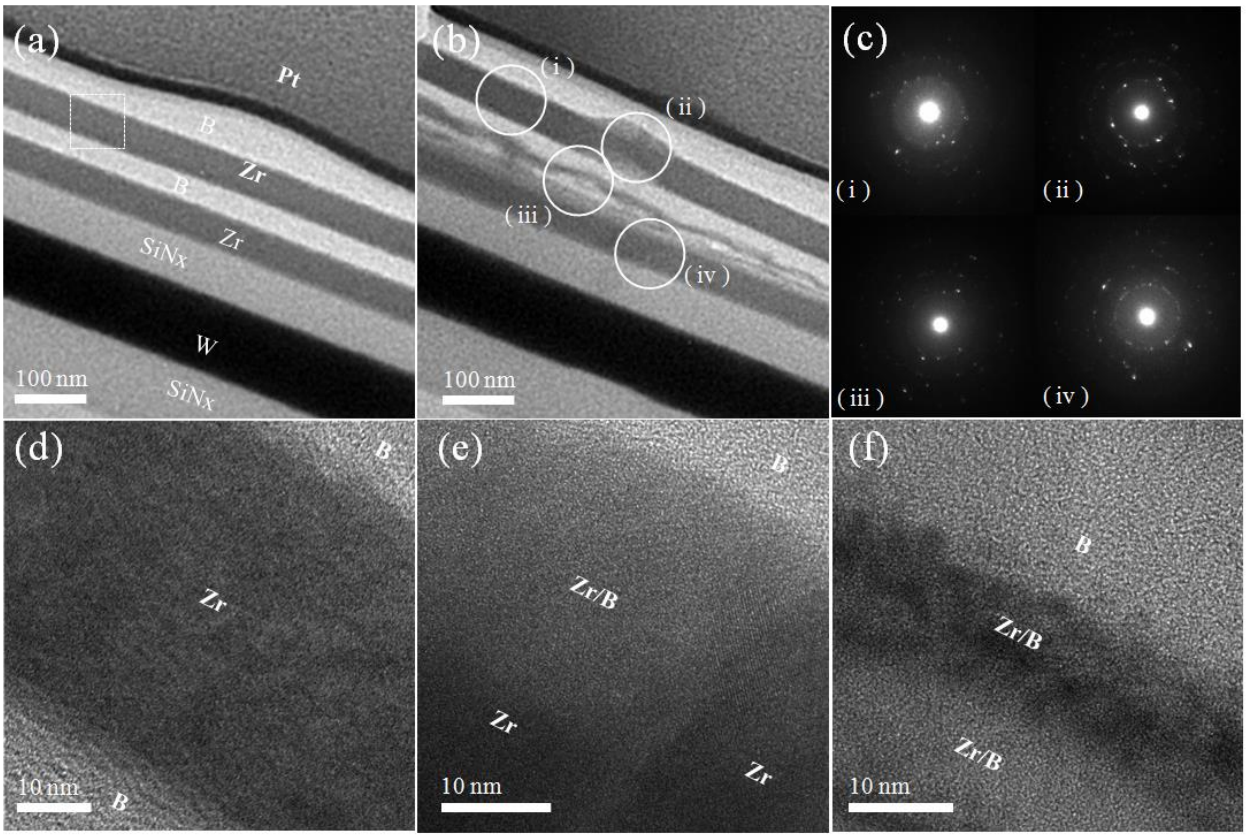

Fig. 5. Cross-section TEM micrographs of a Zr/B multilayer heated up to 450°C. The specimen consists of parts with either narrow (a) or wide (b) inter-diffused layers. (c) Diffraction patterns obtained from the corresponding circled areas in (b) High-resolution images in (d), (e), and (f) were obtained from the inset in (a) and from (ii), (iii) in (b), respectively.

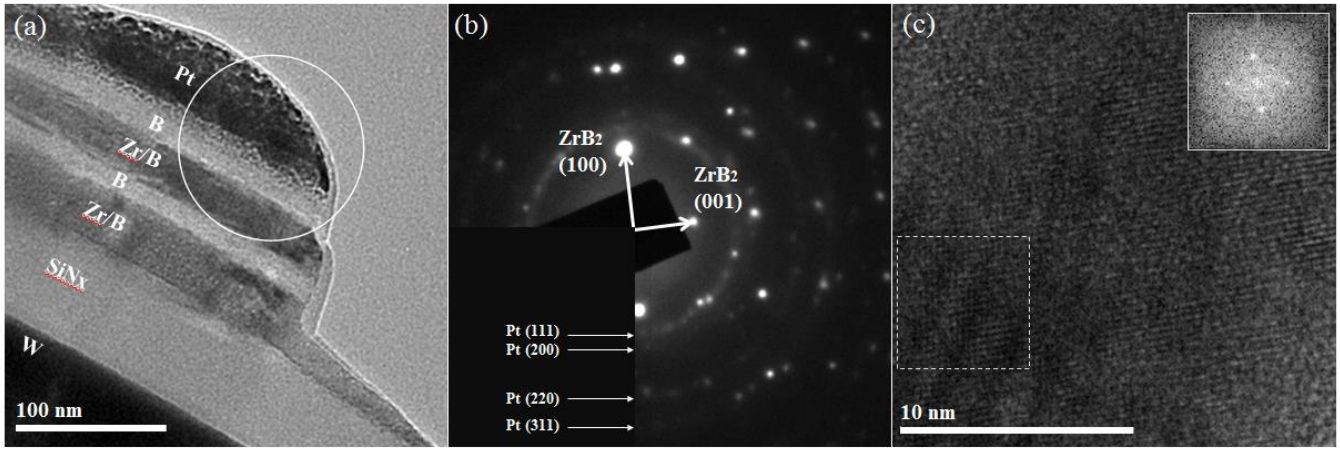

Fig. 6. (a) TEM micrograph of a Zr/B multilayer heated up to 950°C. (b) Electron diffraction pattern obtained from the circled area in (a). Diffraction spots for ZrB_2 and for nano-crystalline Pt are clearly visible. (c) HRTEM image of a crystalline Zr in the same sample. The inset in the figure shows the Fourier transformation of the dashed box.

Fig. 6 shows TEM micrographs for the Zr/B multilayer sample that was used for the nanocalorimetry measurements. The bright-field TEM micrograph in Fig. 6(a) demonstrates that the microstructure of the sample is not homogeneous, even after heating to 950°C. It consists of dark Zr/B layers along with some unreacted B. Electron diffraction measurements on the dark layers in Fig. 6(a) show that this layer contains a mixture of ZrB_2 and Zr grains. The selected area diffraction pattern in Fig. 6(b), for instance, agrees well with the Powder Diffraction File #751050 for ZrB_2, but HRTEM micrographs (Fig. 6(c)) obtained at other locations in the same sample showed crystalline Zr (Powder Diffraction File #050665). No other ZrB-phases were observed. The micrographs indicate that the second stage of the multilayer reaction consists of the formation of crystalline ZrB_2 from the amorphous Zr/B mixture that forms in the first stage. Given that the Zr/B layer consists of both Zr and ZrB_2, it is likely that scans to even higher temperatures would result in the formation of additional ZrB_2, although the

micrographs suggest that the samples had an excess of B, which would prevent total conversion to ZrB_2.

VII. Discussion

The scanning AC nanocalorimetry measurements have clearly identified two distinct stages in the Zr/B solid-state reaction: an exothermal reaction that occurs over a broad range of relatively low temperatures and an elevated-temperature exothermic reaction that occurs over a narrow range of temperatures. We attribute the first reaction to inter-diffusion of Zr and B and the formation of an amorphous Zr/B alloy. There is no evidence that any crystalline Zr-B compounds form at this stage. The amorphous alloy seems to form at certain preferred sites at the Zr/B interfaces resulting in a very non-uniform distribution of the alloy. Heterogeneous diffusion in multilayers has been observed in other multilayers that alternate amorphous and crystalline layers. In particular multilayers coatings that consist of crystalline Ni and amorphous NiP_y alloys show limited inter-diffusion and do not completely homogenize on annealing [29]. The extent of diffusion in these multilayers is controlled by the crystalline layer and by the rate at which P diffuses into the Ni grain boundaries in particular. We suggest here that the broad range of Zr grain sizes from just a few nanometers to several tens of nanometers is responsible for the heterogeneous diffusion of B. If B diffuses predominantly along the Zr grain boundaries, the amorphous Zr/B alloy is expected to form in the regions with nano-crystalline Zr, while regions with larger Zr grains should have much lower B concentrations. The fact that the diffusion process occurs over a broad range of temperatures further suggests that diffusion occurs via a range of pathways with a distribution of relatively low activation energies – a thermally activated process with a well defined activation energy results in a sharp peak in a calorimetry trace obtained at constant scan rate.

The TEM images show that the second stage in the solid-state reaction is associated with the formation of crystalline ZrB_2. The conversion to ZrB_2 is not complete, however, and significant amounts of Zr and B remain. Specifically ZrB_2 grains form in some areas of the sample and not in others. It is likely then that the ZrB_2 grains grow only in those areas of the sample that form the amorphous Zr/B alloy during the first stage, i.e., the second stage corresponds to the crystallization of the amorphous Zr/B alloy formed in the first stage. This observation implies that the microstructure of the Zr layers is critical to obtaining full conversion to ZrB_2, at least in the temperature range considered in this study. Fig. 3b shows that crystallization of the amorphous Zr/B alloy is associated with a decrease of the heat capacity of the sample. While the heat capacity of ZrB_2 is nearly the same as the heat capacity of the equivalent amount of crystalline Zr and B [30, 31], the figure suggests that the heat capacity of the amorphous phase is larger than that of ZrB_2.

A recent study on reactive hot pressing of Zr and B powders using differential thermal analysis [32] showed that the reaction between Zr and B occurs over a broad temperature range from 300 to 900°C, following a two-step process. It is likely that this process also consists of a combination of inter-diffusion and crystallization processes, although diffusion in this case may be controlled by the presence of a native oxide on the Zr grains. Calorimetric studies of the solid-state reactions in Nb/Al multilayers have also revealed double peaks similar to those observed for Zr/B in this study. In the case of Nb/Al, however, the first peak is the result of an interface-limited reaction, while the second peak is associated with a diffusion-limited reaction regime [33].

The enthalpy of the Zr/B solid-state reaction is estimated at 36 kJ/mol, which is significantly smaller than the value of 297 – 323 kJ/mol reported in theoretical and experimental studies on ZrB_2 [4, 34]. The low value of the enthalpy is consistent with the incomplete reaction of B and Zr observed in the TEM and suggests that only about 12% of the sample reacted to form ZrB_2. Although it is difficult to

confirm the conversion rate quantitatively in the TEM, we believe that this number slightly underestimates the actual conversion rate because of some intermixing of Zr and B during the deposition process as observed in the unreacted sample. The largest source of error in the conversion rate is the noise in the PnSC voltage measurements (0.1%), which causes an error of approximately 10% in the enthalpy flow. The uncertainty in the mass of the multilayer sample is estimated at 8%. Given that the Zr/B reaction is very exothermic [4, 34], it may be possible to use Zr/B multilayers as a heat source [24-28] for brazing of ultrahigh-temperature ceramics. For this application, it will be necessary, however, to significantly increase the conversion rate of the reaction through optimization of the multilayer deposition process. The conversion rate may be further enhanced by increasing the total thickness of the sample, which would reduce the heat loss relative to the reaction enthalpy and thus allow the sample to reach a higher temperature.

Finally, it should be pointed out that scanning AC nanocalorimetry combined with the relatively simple data reduction method described in this article is a promising technique for the characterization of reactions in reactive multilayers and of solid-state reactions more generally. The technique provides the same thermodynamic information for thin films as macroscopic calorimetry – one of the most useful tools in the study of materials – for bulk materials. Furthermore, scanning AC nanocalorimetry can access a very wide range of scanning rates making it a useful tool for kinetics studies.

VIII. Conclusions

AC nanocalorimetry combined with the data reduction procedure discussed in the present article makes it possible to measure both heat capacities and reaction enthalpies for thin-film samples, making it the ideal tool for studying solid-state reaction in multilayer samples. This technique has been applied to characterize the Zr/B multilayer reaction. The reaction proceeds in two stages, both of which are exothermic: inter-diffusion of Zr and B resulting in an amorphous Zr/B alloy and crystallization of this alloy to form ZrB_2. The inter-diffusion process occurs in a heterogeneous fashion at relatively low temperatures, while the crystallization process occurs at more elevated temperatures. As the ZrB_2 formation reaction is very exothermic, Zr/B multilayers may be useful in brazing applications of high-temperature ceramics, provided the conversion rate can be further improved through optimization of the multilayer deposition process.

Acknowledgement

This work was supported by the Air Force Office of Scientific Research under Grant FA9550-12-1-0098. It was performed in part at the Center for Nanoscale Systems at Harvard University, which is supported by the National Science Foundation under Award No. ECS-0335765, and at Materials Research Science and Engineering Center at Harvard University, which is supported by the National Science Foundation under Award No. DMR-0820484.

Appendix

In this appendix, we provide an estimate of the conduction losses through the membrane and the heating element. Let *y* be the coordinate in the direction perpendicular to the heating element (See Fig. 1c). The temperature distribution in the membrane is then described by the one-dimensional thermal diffusion equation [19],

$$\rho c_P \frac{\partial T}{\partial t} = k \frac{\partial^2 T}{\partial y^2} - 2\frac{\varepsilon\sigma}{h}\left(T^4 - {T_0}^4\right), \tag{A1}$$

with conditions

$$\begin{aligned} T(y,0) &= T_0, \\ T(0,t) &= T_0 + f(t), \\ T(\infty,t) &= T_0, \end{aligned} \tag{A2}$$

where ρ, c_p, k, ε, and h designate the mass density, heat capacity, thermal conductivity, emissivity, and thickness of the membrane; σ is the Stefan-Boltzmann constant. The function *f(t)* describes the temperature history of the heating element. Defining $\tau = T - T_0$,

$$\alpha = \frac{k}{\rho c_p}, \tag{A3}$$

$$\beta = \frac{8\varepsilon\sigma {T_0}^3}{h\rho c_p}, \tag{A4}$$

and performing a linear expansion of the radiation term in Eq. (A1) leads to the following equation

$$\frac{\partial \tau}{\partial t} = \alpha \frac{\partial^2 \tau}{\partial y^2} - \beta\tau, \tag{A5}$$

with conditions

$$\tau(y,0) = 0,$$

$$\tau(0,t) = f(t), \tag{A6}$$

$$\tau(\infty,t) = 0.$$

The solution of this equation can be written as [19]

$$\tau(y,t) = \int_0^t f(t')K(t-t')dt', \tag{A7}$$

where

$$K(t-t') = \frac{y\exp\left[\frac{-y^2}{4\alpha(t-t')} - \beta(t-t')\right]}{2\sqrt{\pi\alpha}(t-t')^{3/2}}. \tag{A8}$$

The integral in Eq. (A7) is difficult to calculate numerically for arbitrary functions *f(t)*. Here we describe a simple method to evaluate the integral for an experimentally measured temperature history based on the realization that the integral is analytical for a linear temperature history. Specifically, if the experimental temperature history consists of a set of *n* data points (t_i, T_i) and is represented by a linear spline, the temperature profile at time t_n is well approximated by

$$\tau(y,t) = \sum_{i=1}^{n-2}\int_{t_i}^{t_{i+1}}(A_i + B_i t')K(t-t')dt' + \int_{t_{n-1}}^{t_n}(A_{n-1} + B_{n-1}t')K(t-t')dt', \tag{A9}$$

where

$$A_i = \frac{T_i t_{i+1} - T_{i+1}t_i}{t_{i+1}-t_i} \text{ and } B_i = \frac{T_{i+1}-T_i}{t_{i+1}-t_i}. \tag{A10}$$

The heat lost by conduction into the membrane is then given by

$$L_C = 2kA\frac{\partial\tau}{\partial y}\Big|_{y=0}$$

$$= 2kA\left(\sum_{i=1}^{n-2}\frac{\partial}{\partial y}\left(\int_{t_i}^{t_{i+1}}(A_i + B_i t')K(t-t')dt'\right)\Big|_{y=0} + \frac{\partial}{\partial y}\left(\int_{t_{n-1}}^{t_n}(A_{n-1} + B_{n-1}t')K(t-t')dt'\right)\Big|_{y=0}\right)$$

$$= 2kA\left(\sum_{i=1}^{n-2} I_i + I_{n-1}\right), \quad \text{(A11)}$$

where A is the total cross-sectional area of the membrane. The integrals in Eq. (A11) can be evaluated analytically leading to the following expressions for I_i ad $I_{n\text{-}1}$

$$I_i = (A_i + B_i t_n)\frac{1}{\sqrt{\alpha\pi}}\left\{\frac{e^{\beta(t_{i+1}-t_n)}}{\sqrt{t_n - t_{i+1}}} - \frac{e^{\beta(t_i-t_n)}}{\sqrt{t_n-t_i}} + \sqrt{\beta\pi}\left(erf\left(\sqrt{\beta(t_n-t_{i+1})}\right) - erf\left(\sqrt{\beta(t_n-t_i)}\right)\right)\right\} +$$

$$\frac{B_i}{2\sqrt{\alpha\beta}}\left(erf\left(\sqrt{\beta(t_n-t_{i+1})}\right) - erf\left(\sqrt{\beta(t_n-t_i)}\right)\right), \quad \text{(A12)}$$

And

$$I_{n-1} = -(A_{n-1} + B_{n-1}t_n)\frac{1}{\sqrt{\alpha\pi}}\left\{\frac{e^{\beta(t_{n-1}-t_n)}}{\sqrt{t_n - t_{n-1}}} + \sqrt{\beta\pi}erf\left(\sqrt{\beta(t_n-t_{n-1})}\right)\right\} - \frac{B_{n-1}}{2\sqrt{\alpha\beta}}erf\left(\sqrt{\beta(t_n-t_{n-1})}\right). \quad \text{(A13)}$$

Substituting Eqs. (A12) an (A13) into Eq. (A11) results in an expression that can be used to estimate the conductive heat loss through the membrane at a time t_n from the prior temperature history of the heating element. Evaluation of this expression requires knowledge of the parameters α and β, which are readily determined experimentally [19]. The main approximation in the analysis is the linear expansion of the thermal radiation loss in Eq. (A5). This approximation is acceptable as long as the neglected radiation loss terms are small compared to the other terms in the equation, i.e., $\tau \ll T_o/\beta t$, where t is the time scale of the experiment. Given the approximate character of the analysis, the preferred method of eliminating the conduction loss from experimental nanocalorimetry data is to take the difference between two subsequent scans with similar thermal histories. The above analysis can then be applied as a small correction to account for the difference in conduction loss as a result of the slight difference in thermal history between the two scans. That is the approach taken in this study.

Finally, the conduction loss through the heating element can be estimated using a similar approach. Because the element generates heat, it is necessary to include a volumetric power term in the left hand side of Eq. (A1)

$$\rho c_P \frac{\partial T}{\partial t} = k \frac{\partial^2 T}{\partial x^2} - 2\frac{\varepsilon\sigma}{h}\left(T^4 - {T_0}^4\right) + P_v, \tag{A14}$$

where the physical constants now refer to the composite properties of the heating element and the membrane. The volumetric power changes with temperature through the temperature-dependence of the resistivity of the heating element

$$P_v = P_o(1 + \lambda\tau), \tag{A15}$$

so that Eq. (A14) can be reduced to

$$\frac{\partial \tau}{\partial t} = \alpha \frac{\partial^2 \tau}{\partial x^2} - \left(\beta - \frac{P_o \lambda}{\rho c_p}\right)\tau + \frac{P_o}{\rho c_p}. \tag{A5}$$

Writing this equation for the temperature difference between two subsequent scans eliminates the last term on the right hand side of the equation and an equation of the type (A5) is recovered. As long as P_o is constant and $P_o < \beta\rho c_p/\lambda$, the same approach can be used to calculate the conduction loss through the heating element as for the membrane.

References

1. W.G. Fahrenholtz, G.E. Hilmas, I.G. Talmy, and J.A. Zaykoski, J. Am. Ceram. Soc. **90**,1347 (2007).
2. K. Upadhya, K. Yang, and W. Hoffman, Am. Ceram. Soc. Bull. **76**, 51 (1997).
3. E. Wuchina, E. Opila, M. Opeka, W. Fahrenholtz, and I. Talmy, Electrochem. Soc. Interface. **16,** 30 (2007).
4. P. Vajeeston, P. Ravindran, C. Ravi, and R. Asokamani. Phys. Rev. B **63**, 045115 (2001).
5. Guo S. J, Eur. Ceram. Soc. **29**, 995 (2009).
6. S.K. Mishra, S. Das S, S.K. Das, P. Ramachandrarao, J. Mater. Res. **15**, 2499 (2000).
7. M. Brochu, B. Gauntt, T. Zimmerly, A. Ayala, and R. Loehman, J. Am. Ceram. Soc. **91**, 2815 (2008).
8. S. Guo, T. Nishimura, and Y. Kagawa, Scr. Mater. **65**, 1018 (2011).
9. A.L. Chamberlain, W.G. Fahrenholtz, and G.E. Hilmas, J. Eur. Ceram. Soc. **29**, 3401 (2009).
10. S. Guo, C. Hu, and Y. Kagawa, J. Am. Ceram. Soc. **94**, 3643 (2011).
11. F. Spaepen and C.V. Thompson, Appl. Surf. Sci. **38**, 1 (1989).
12. C. Michaelsen, K. Barmak, and T.P. Weihs, J. Phys. D: Appl. Phys. **30**, 3167 (1997).
13. K. Barmak, C. Michaelsen, and G. Lucadamo, J. Mater. Res. **12**, 133 (1997).
14. K.J. Blobaum, D. Van Heerden, A.J. Gavens, and T.P. Weihs, Acta Mater. **51**, 3871 (2003).
15. M. Vohra, M. Grapes, P. Swaminathan, T.P. Weihs, and O.M. Knio, J. Appl. Phys. **110**, 123521 (2011).
16. Y. Motemani, P.J. McCluskey, C. Zhao, M.J. Tan, and J.J. Vlassak, Acta Mater. **59**, 7602 (2011).
17. E.A. Olson, M.Y. Efremov, M. Zhang, Z. Zhang, and L.H. Allen, J. Microelectromechanical Syst. **12**, 355 (2003).
18. P.J. McCluskey and J.J. Vlassak, J. Mater. Res. **25**, 2086 (2010).
19. P.J. McCluskey and J.J. Vlassak, Thin Solid Films **518**, 7093 (2010).
20. K. Xiao, J.M. Gregoire, P.J. McCluskey, and J.J. Vlassak, Rev. Sci. Instrum. **83**, 114901 (2012).

21. H. Huth, A.A. Minakov, and C. Schick, J. Polym. Sci. Part B Polym. Phys. **44**, 2996 (2006).

22. K. Xiao, J.M. Gregoire, P.J. McCluskey, D. Dale, and J.J. Vlassak, J. Appl. Phys. **113**, 243501 (2013).

23. J.M. Gregoire, K. Xiao, P.J. McCluskey, D. Dale, G. Cuddalorepatta, and J.J. Vlassak, Appl. Phys. Lett. **102**, 201902 (2013).

24. J. Wang, E. Besnoin, A. Duckham, S.J. Spey, M.E. Reiss, O.M. Knio, M. Powers, M. Whitener, and T.P. Weihs, Appl. Phys. Lett. **83**, 3987 (2003).

25. A. Duckham, S.J. Spey, J. Wang, M.E. Reiss, T.P. Weihs, E. Besnoin, and O.M. Knio, J. Appl. Phys. **96**, 2336 (2004).

26. J. Wang, E. Besnoin, O.M. Knio, and T.P. Weihs, Acta Mater. **52**, 5265 (2004).

27. A.J. Swiston Jr., T.C. Hufnagel, and T.P. Weihs, Scr. Mater. **48**, 1575 (2003).

28. X. Qiu and J. Wang, Sensors Actuators Phys. **141**, 476 (2008).

29. C.A. Ross, D.T. Wu, L.M. Goldman, and F. Spaepen, J. Appl. Phys. **72**, 2773 (1992).

30. J.W. Zimmermann, G.E. Hilmas, W.G. Fahrenholtz, R.B. Dinwiddie, W.D. Porter, and H. Wang, J. Am. Ceram. Soc. **91**, 1405 (2008).

31. R.C. Weast, *CRC handbook of chemistry and physics* (CRC Press, Cleveland, Ohio, 1977).

32. A.L. Chamberlain, W.G. Fahrenholtz, and G.E. Hilmas, J. Am. Ceram. Soc. **89**, 3638 (2006).

33. K.R. Coffey, L.A. Clevenger, K. Barmak, D.A. Rudman, and C.V. Thompson, Appl. Phys. Lett. **55**, 852 (1989).

34. E.J. Huber, E.L. Head, and C.E. Holley, J. Phys. Chem. **68**, 3040 (1964).